Horizontally Arranged Zinc Platelet Electrodeposits Modulated by Fluorinated Covalent Organic Framework Film for High-Rate and Durable Aqueous Zinc Ion Batteries

Zaiping Guo (Zaiping.guo@adelaide.edu.au)
The University of Adelaide
Zedong Zhao
Fudan University
Rong Wang
Fudan University
Chengxin Peng
University of Shanghai for Science and Technology
Wuji Chen
Fudan University
Tianqi Wu
Fudan University
Bo Hu
Fudan University
Jiaxi Zeng
Fudan University
Peiying Liu
Fudan University
Yicheng Liu
Fudan University
Jia Guo
Fudan University
Hongbin Lu
Fudan University https://orcid.org/0000-0001-7325-3795

Article

Keywords: batteries, catalysis, energy, rechargeable aqueous zinc-ion batteries (RZIBs)

DOI: https://doi.org/10.21203/rs.3.rs-494431/v1

Version of Record: A version of this preprint was published at Nature Communications on November 16th, 2021. See the published version at https://doi.org/10.1038/s41467-021-26947-9.

Abstract

Rechargeable aqueous zinc-ion batteries (RZIBs) provide a promising complementarity to the existing lithium-ion batteries due to their low cost, non-toxicity and intrinsic safety. However, Zn anodes suffer from zinc dendrite growth and continuous unfavorable side reactions, resulting in low Coulombic efficiency (CE) and severe capacity decay. Here, we develop an ultrathin, fluorinated two-dimensional porous covalent organic framework (FCOF) film as a protective layer on the Zn surface to address these issues. The strong interaction between fluorine (F) in FCOF and Zn reduces the surface energy of the Zn (002) crystal plane and regulates planar growth of zinc anode materials. As a result, Zn deposits underneath FCOF films show parallel platelet morphology with (002) planar orientations preferred. Furthermore, F-containing nanochannels facilitate the de-solvation of hydrated Zn ions and prevent electrolyte penetration, thus retarding corrosion of Zn. Such unique FCOF films prolonged the Zn symmetric cell lifespan to over 1700 h, which is 13 times longer than the cells without protection (125 h). The assembled full cells demonstrate a cycle life of over 250 cycles at 3 $mAcm^{-2}$ under practical conditions, including lean electrolyte (12 $\mu LmAh^{-1}$), limited Zn excess (only 1×excess), and a high mass loading of MnO_2 cathode (16 $mgcm^{-2}$). This work provides a new perspective for the realization of planar deposition of zinc metal anodes for developing high performance Zn-based batteries.

Introduction

Zinc (Zn) anode-based aqueous batteries are attracting tremendous interest owing to Zn's high theoretical capacity (820 mAh/g), low potential (-0.762V versus the standard hydrogen electrodes), high natural abundance, low cost, and intrinsic non-flammable advantage over organic-based lithium batteries[1-3]. Unfortunately, previous Zn anodes showed poor reversibility in aqueous electrolytes[1,4,5]. Issues including Zn dendrite formation, continuous parasitic hydrogen evolution reaction (HER), and irreversible by-products, resulting in low Coulombic efficiency (CE), and shortened battery life[6-9]. To stabilize the Zn anode, various strategies including electrolyte optimization (additives[10] and water-in-salt[1]/gel electrolytes[11]), surface coating materials (*e.g.* metal-organic frameworks[12], polyamide[8] and ZnO networks[6]) and Zn bulk structure engineering (*e.g.* CNT frameworks[13] or zinc-aluminum alloy[14]) have been proposed to achieve higher performance Zn anodes. However, there are still some unsolved issues with these strategies, which restricts them to subdued performance levels in Zn batteries. For instance, manipulating previous electrolyte compositions leads to an increase in overall costs[15], sacrifices rate performance of the batteries owing to their slow ionic conductivity and the HER is only lowered, not eliminated[2]. Interfacial modification layers are effective for suppressing HER[8,16], however, the huge volume change during repeated Zn plating/stripping can damage protective layers, even peeling them completely off the Zn matrix[17]. Employing conductive 3D hosts could help to realize high-rate Zn deposition[13,18], but adds additional porosity and weight, thereby reducing the volumetric/gravimetric energy density of the batteries. Therefore, developing alternative techniques to achieve dendrite-free Zn anodes while maintaining fast Zn deposition is urgently needed.

The crystallinity and morphology of Zn electrodeposits dominates the reversibility of Zn plating/stripping[5,19,20], yet the linkage has often not been considered. Modulating irregularly-shaped Zn to planar Zn electrodeposits is desirable for high reversibility of Zn anodes[5]. The electrodeposition processes of Zn, which involve crystallization, exhibit a direct correlation to the morphology of deposits[20]. Upon plating, the influences of external factors often promote the preferred orientation of Zn grains along a specific crystal plane, thus leading to a specific morphological "texture"[21-23]. The morphology and texture of Zn deposits have been proved to be closely related to additives[22,24-26], initial substrate composition and texture[5,27,28], and applied external fields[19,29]. Organic molecules and additives can adsorb on a Zn surface, guiding the Zn deposits to show specific preferred orientation of crystal planes[25,26,30]. For example, the polyethylene-glycolin electrolytes[25] make the Zn deposits show a preferred orientation exposure of (002) and (103) planes, which mitigates dendrite formation and reduces the later corrosion rates. Substrate such as stainless steel modified with an aligned graphene layer[5], shows good lattice matching with Zn, which induces epitaxial deposition of Zn along the (002) planes, achieving ultra-long cycling life. Recently, fields generated by rotating disc electrodes[19] are reported to promote the crystallographic reorientation of Zn to be grow parallel to the substrate, and the reversibility of Zn deposition/stripping is greatly increased. Therefore, correlating the crystallography and morphology to deeply understand and regulate the electrodeposition behavior of Zn is of great significance for developing long-life Zn batteries. However, there is an obvious lacks of fundamental elucidation of the mechanism controlling planar Zn deposition. Furthermore, the surface stability of inorganic crystals has long been thought to be dominated by their surface energy[31-33]. From the perspective of crystal growth, controlling the surface energy of Zn crystal planes offers exciting opportunities to realize planar zinc deposition.

Here, by using two-dimensional (2D) covalent organic frameworks (COF) as a multi-functional platform (Fig.**1**a)., we develop a mechanically strong, ultra-thin, and fluorinated COF (FCOF) film as a protective layer on Zn anode surfaces (FCOF@Zn). Benefiting from the tailored functional group and ordered nanochannels of the COF, F atoms that evenly distribute within the nanopores endow the film with two striking features (Fig.**1**b): 1) the hydrophobic F atoms promote the de-solvation of hydrated zinc ions (Zn^{2+}) and accelerate Zn^{2+} transport at the electrolyte/Zn anode interface. The FCOF film is also found to be effective in preventing electrolyte penetration toward the Zn surface, thus mitigating the corrosion rate, and 2) the electronegative F atoms show strong interaction with the underlying Zn atoms, leading to a lower surface energy of Zn (002) planes compared to that of conventional Zn (101) planes. Consequently, Zn deposits show platelet morphology with preferred orientation along the (002) plane, and the platelets are arranged parallel to each other, which realizes a planar Zn deposition morphology. Compared with bare Zn anodes, the FCOF@Zn anodes show prolonged cycle life and better reversibility in a large current density range (5-80 mA/cm^2). The assembled full cells paired with manganese dioxide (MnO_2) cathodes a show stable cycle life for over 250 cycles under practical condition of lean electrolyte, high areal capacity cathode and limited Zn excess.

Results

Synthesis and characterization of the FCOF film.

The imine-linked FCOF thin films were prepared through a solvothermal procedure (Fig.**2**a). In a typical process, two monomers (2,3,5,6-tetrafluoroterephthaldehyde (TFTA) and 1,3,5-tris (4-aminophenyl) benzene (TAPB)), are dissolved in a dioxane/mesitylene (D/M) mixture and condensed in a solvothermal tube, using acetic acid as the catalyst. To obtain a highly crystalline and continuous FCOF film, reaction conditions *i.e.* the proportion of solvent mixture, the concentration of catalyst and the reaction time needs to be controlled (Supplementary Fig. 1-4). When the ratio of D: M solvent in the mixtures is optimized to 1:9 (v/v) with 1.5M acetic acid catalyst, continuous bright orange FCOF films without any insoluble COF particulates are uniformly attached to the tube inner wall, indicating the FCOF films is successfully achieved (Supplementary Fig. 1). After soaking in pure water overnight, the free-standing FCOF films detach from the tube wall due to surface tension (Supplementary Fig. 5). The growth mechanism of FCOF film during solvothermal processes is mainly attributed to the fusion of numerous nanospheres that are formed during a co-condensation reaction (Supplementary Fig. 2), as revealed by the time-dependent morphology evolution (Supplementary Fig. 4). In addition, such uniform FCOF films can grow on various substrates such as copper (Cu), silicon, stainless steel foil/grids, nickel and titanium foils by placing the targeted substrates in the reaction solutions, as shown in Supplementary Fig. 6. This is beneficial for structural and property characterization after being transferred to various substrates during subsequent post-processing.

The crystal structure of the FCOF film is identified by two-dimensional wide-angle X-ray scattering (2D WAXS) measurement (Fig. **2**b). From the integrated WAXS curves, the peaks at q=0.20, 0.35, 0.40, 0.53 A^{-1} correspond to the planes (100), (110), (200) and (210), respectively, consistent with a previous report[34], confirming the high degree of crystallinity of the as-prepared film. High-resolution transmission electron microscopy (HRTEM) images clearly show the lattice fringes of the FCOF film at a spacing of ~0.34nm (Fig. **2**c), which represents the π-π stacking distance. Field emission scanning electron microscopy (FESEM) images showed a smooth and defect-free film suspended on a copper grid (Fig. **2**d), and the folds at the edges also reflect the flexibility of the film to a certain extent (Fig. **2**e). Brunauer-Emmett-Teller (BET) measurement indicates the surface area of the film is as high as 723 m^2g^{-1}, and the main pore size distribution is 2-3 nm in diameter (Fig. **2**f), which is well consistent with the WAXS result. The chemical structure of the FCOF film was further confirmed. The emerging peak at 1614 cm^{-1} in FTIR spectra (Fig. **2**h) is assigned to the newly formed C=N imine stretch vibrations. The peak intensity at 1705 cm^{-1} assigned to C=O stretching weakens in FCOF film, indicating the consumption of the aldehyde groups of TFTA monomers[34]. High-resolution X-ray photoelectron spectroscopy (XPS) of the N_{1s} spectra (Fig. **2**g) shows that the weak peak at 399.89 eV arises from the N-H bonds[35], revealing the small amount of residues of the amino groupss[34], consistent with the FTIR result (N-H peak at ~3400 cm^{-1}). The high intensity of the peak at 398.96eV in the N_{1s} spectra (Fig. **2**g) further confirm the formation of C=N (imine)

The F atoms are the crucial elements within the FCOF films for achieving high-performance Zn anodes. The element mapping obtained from energy dispersive X-ray spectroscopy (EDX) indicates that F is evenly distributed in the film (Supplementary Fig.7). The F content is estimated to be 8.25 atomic %, in according to the XPS result (Supplementary Fig.8). In addition, the thickness of the film is adjustable by means of controlling the concentration of monomers. As determined by AFM analysis, the FCOF films had thicknesses of ~100, ~300 and ~500nm (Supplementary Fig. 9). The FCOF@Zn anode is fabricated *via* a pulling method in acetone solvent using Zn foil as substrate. After drying, the FCOF film tightly adhered the surface of the Zn foil and did not detach even under rolling, bending or unfolding of the Zn (Fig. **2**j, 2i). In addition, as determined by nano-indentation measurements (Fig. **2**k), the high quality two-dimensional FCOF crystalline films showed a remarkable elastic modulus exceeding 30GPa and an average hardness of over 1.2GPa, which is an order of magnitude higher than a recently reported TiO_2 and polyvinylidene difluoride (PVDF) hybrid matrix[36] (2.67GPa). The good mechanical strength is greatly beneficial to buffer volume expansion and retard dendrite propagation during the dissolution/deposition of Zn anodes.

Good Zn^{2+} conductivity through a protective layer is highly desired for Zn anodes. To experimentally determine the ion transport behavior of the FCOF films, the ionic conduction was calculated based on electrochemical impedance spectroscopy (EIS) results (Supplementary Fig.10 a and b). The ion conductivity (24.19 mS/cm) for the 100nm FCOF film coated glass fiber separator is 1.7 times higher than the bare glass fiber separator (14.12mS/cm). The result indicates that Zn^{2+} transport is enhanced by the FCOF film[37,38]. According to the equivalent circuit fitting results (Supplementary Fig.10 c and d), Zn anodes coated by the FCOF films with different thicknesses revealed lower charge transfer resistance (R_{ct}) than bare Zn. In particular, the R_{ct} of Zn anodes coated by the 100 nm thick FCOF film is lowest (90 Ω), about half that of bare Zn (180 Ω). Apparently, the Zn^{2+} transport is increased by the fluorinated 1D nanochannels. This is mainly due to the F atoms surrounded within the nanopores that endow the film a strong hydrophobic effect. Consequently, the fluorinated nanochannels inside the FCOF film appear to assist the de-solvation of hydrated Zn^{2+}, thereby increasing the Zn^{2+} transport[39]. This is further supported by the Zn^{2+} transference number (ZTN) tests (Supplementary Fig.11), wherein the FCOF films show a higher ZTN (0.7) compared with conventional glass fiber separators (0.4).

In addition, the FCOF film is beneficial for aqueous electrolyte (2M $ZnSO_4$) corrosion resistance of the Zn surface. The impedance of the FCOF@Zn symmetric cells increases from 180 to 600Ω within 8 hours (h) after cell assembly (Supplementary Fig. 12a). For bare Zn symmetric cells, on the contrary, the impedance increases dramatically from 200 to over 10000 Ω after 8 h (Supplementary Fig. 12b). The increase in impedance implies that the continuous corrosion of Zn by the electrolyte results in large amounts of by-products deposited on the surface. Time-dependent XRD patterns (Supplementary Fig.12c) show a peak at around 8° appears, corresponding to the by-product species $Zn_4SO_4(OH)_6{\cdot}5H_2O$ (JCPDS# 39-0688)[11]. When plain Zn anodes are immersed in aqueous electrolyte for 48 h, the peak intensity of by-products increases sharply. Much less irreversible by-product is accumulated on the surface of FCOF@Zn anodes

Horizontal Parallel Zn platelet deposition enabled by the FCOF film.

In addition to the fast ion conduction and suppression of side reactions features, the morphology and texture of Zn deposits has been proven to have large impact on the cycling life of Zn batteries. Attaining an even planar deposition can ensure the batteries running for a prolonged time without short circuiting. To investigate the deposition morphology of Zn underneath the FCOF film, the Ti/Zn or FCOF@Ti cells are employed. As shown in Fig. **3**a, b, the Zn deposits underneath the FCOF film exhibits platelet morphology and the platelets are stacked horizontally in response to a controlled capacity of 1mAh/cm^2. Meanwhile, for the bare Ti without FCOF film protection (Fig. **3**c, d), disordered, distributed and irregularly-shaped Zn dendrites are observed on the surface. When further increasing the used capacity to 2mAh/cm^2, similar consistent morphological characteristics of the two samples are still maintained. The XRD results reveal the intensity of (002) plane located at 2θ=36.3° is highest for the Zn deposits underneath FCOF films (Fig. **3**e, f), while the bare Zn deposits show (101) planes dominating the peak intensities (Fig. **3**g, h). This change in the dominant peaks implies that the FCOF films on Zn anodes influence the preferred orientation of the Zn deposits. The orientation of the Zn deposits can also be quantified by calculating the texture coefficient[40,41] (Tc, Supplementary Fig. 13). The Tc(002) of Zn deposits underneath the FCOF film is 19.2, much higher than that of the deposits on bare Zn (11.5), verifying the preferential growth on the (002) plane of Zn modulated by an FCOF film. X-ray diffraction pole figures were used to further identify the texture information of Zn deposits. The (002) pole figure (Fig. **3**k) of Zn underneath FCOF films shows a sharp intensity concentration around ψ = 0-20°, indicating that the Zn platelets have a preferred textured based on (002) planes, and are nearly paralleled to the electrode substrate[24,42] (Fig. **3**i). In contrast, the random distributed of bare Zn deposits leads to a broad distribution of grain orientations, and the corresponding (002) pole figure (Fig. **3**j) shows almost uniform distribution of diffraction intensity along the radial direction, indicating its random (non-preferential) texture.

In addition, the 2D WAXS patterns of deposited Zn underneath FCOF film show some strong, discrete diffraction spots in the ring plane (Fig. **3**l, m), while for bare Zn deposits, the WAXS results are continuous diffraction rings (Fig. **3**n, o). This indicates that the bare Zn deposits are polycrystalline and randomly oriented, whereas the Zn grain size influenced by FCOF films is larger and more oriented[5]. The structure of the Zn platelets was characterized by HRTEM and selected area electron diffraction (SAED). As shown in Fig. **3**p,q and Supplementary Fig. 14, the diffraction patterns of the SAED results can be indexed into diffraction spots of the [001] zone. The HRTEM image of Fig. **3**r further shows two *d*-spacings of 0.230 nm and 0.133 nm with an interfacial angle of 90°, corresponding to the (100) and (1-20) planes, respectively. The HRTEM result is in accord with the indexed SAED diffraction spots. To further verify the indexing results, an atomic arrangement model of Zn along the [001] direction was simulated, as shown in Fig. **3**s. Obviously, the indexed result matches well with the theoretical crystal model. According to the above results, we conclude that the exposed hexagonal planes of the Zn platelet are predominately (002) planes.

Performance evaluation of the high-rate and long-life zinc anode.

The planar Zn deposition morphology, fast Zn^{2+} transport, and corrosion resistance properties enabled by the FCOF film are expected to greatly improve the electrochemical performance of Zn anodes. The reversibility of Zn anodes can be measured by a procedure that wherein a specific amount of Zn is plated on the substrate and then stripped away. Coulombic efficiency (CE) is an important index to evaluate such reversibility. The CE using the half cells in FCOF@Ti/Zn and Ti/Zn configurations is measured. At a moderate current density (1mAhcm^{-2}, 5mAcm^{-2}, Supplementary Fig.15a-c), the FCOF@Ti/Zn cells produced CE values of ~98.4% on average, with stability over 480 cycles. By contrast, the Ti/Zn with no FCOF cells ran for only 30 cycles, and their CE was around ~95.1%. When the current density is increased to an ultrahigh current density of 80 mAcm^{-2}(Fig. **4**a), the FCOF@Ti/Zn cells still exhibited a high CE of approaching 97.2% on average within for 320 cycles, whereas the CE of the Ti/Zn cells decreases rapidly after 95 cycles. When further increasing the capacity to 2mAhcm^{-2} at a current density of 40mAcm^{-2}, the FCOF@Ti/Zn cells showed CE of 97.3% for over 250 cycles, much higher than that of the Ti/Zn cells (~35 cycles, 84.1%). Remarkably, as evidenced from the AFM height and phase imaging (Fig. **3**e, f, Supplementary Fig.16a and c), the horizontally arranged platelet morphology of the Zn deposits underneath FCOF well remained well after 100 cycles during Zn plating/stripping processes (1mAhcm^{-2}, 5mAcm^{-2}). The average height difference (along X and Y axis) is only 170 nm (Supplementary Fig.16e), indicating the surface of the Zn deposits underneath FCOF is very flat and homogeneous. However, the Zn deposits on bare Ti after 100 cycles showed fluctuating and rough patterns with a much higher height difference of 710nm (Supplementary Fig.16b, d and f). During the Zn plating/stripping process, the H^+ from the decomposition of water will receive electrons and then evolve H_2, which could induce an increase of OH^-. The generated OH^- will react with Zn^{2+}, SO_4^{2-}, and H_2O to form by-products such as $Zn(OH)_2$ or $Zn_4SO_4(OH)_6{\cdot}nH_2O$ on Zn surface[16]. Raman spectroscopy was carried out to reveal the components on Zn deposits surfaces after cycling (100 cycles at 1mAh/cm^2, 5mA/cm^2). Sharp peaks at 1152, 1110, 1011 and 967 cm^{-1} are observed on the Zn deposits on bare Ti (Supplementary Fig.17a), which implies that the by-product should be the $Zn_4SO_4(OH)_6{\cdot}5H_2O$[43]. In contrast, the peaks of the Zn deposits underneath FCOF are not obvious and their intensity is much lower (Supplementary Fig.17b), indicating less by-product accumulation on its surface. Raman mapping (8×10μm area, Fig. **4**g) of the dominated peak at 967 cm^{-1} reveals that the counts variation for the Zn deposits underneath FCOF is within 13-726, which is one to two orders of magnitude smaller than for Zn deposits on bare Ti (Fig. **4**h, counts: 1200-8400). It has been reported that the Zn deposits with high percentage of (002) planes parallel to the substrate could provide higher corrosion resistance than other planes[44]. Combined with the F endowed hydrophobic properties, the water-related side reactions could be largely suppressed in the Ti@FCOF@Zn cells. In addition, the bare Ti is not adequate for regulating the zinc deposition behavior or suppressing by-products accumulation, causing elevated voltage hysteresis or short circuiting of the batteries, as evidenced by the voltage fluctuation in Ti/Zn cells during cycling (Supplementary Fig.15c-e). Whereas the voltage files of FCOF@Ti/Zn remained stable at various levels of current density (Supplementary Fig.15a, Fig. **4**c and d). Meanwhile, FCOF@Ti/Zn anodes display long-term stability of

the Zn plating/stripping process even at ultrahigh current density up to 80 $mAcm^{-2}$, larger than that of most previous studies (Supplementary Table 1).

To evaluate the stability of the Zn anodes, the FCOF@Zn symmetric cells showed prolonged cycle life for over 1700h at 1 $mAhcm^{-2}$ and 5 $mAcm^{-2}$, which was nearly 13 times the performance figures of the bare Zn anodes (Fig. **4**i). The FCOF@Zn symmetric cells showed lower voltage hysteresis (FCOF@Zn: 60 mV *vs.* bare Zn: 80 mV), which we mainly attribute to the enhanced Zn^{2+} transport within the 1D fluorinated nanochannels. Under elevated current densities of 8 and ,40$mAcm^{-2}$ (Supplementary Fig.15e and Fig. **4**j), the FCOF@Zn symmetric cells could sustain repeated deposition/dissolution processes without obvious significant fluctuations in the voltage-time curves. However, the bare Zn symmetric cells suffer short-circuits after a few limited cycles. The excellent performance of FCOF@Zn symmetric cells at ultrahigh current density (40$mAcm^{-2}$) is also far superior to most previous reported values (below 10$mAcm^{-2}$, Supplementary Table 2). The highly stable electrochemical performance of the FCOF@Zn anodes indicates that dendrite formation is largely suppressed. To identify the suppression of dendrite growth in FCOF@Zn anode, transparent home-made Zn/Zn symmetric cells with or without FCOF were assembled to realize in situ monitoring of the Zn deposition process using an optical microscope. Zn deposition was performed under a current density of 20$mAcm^{-2}$ for 35 mins. As shown in Fig. **4**k, after an initial 5 mins of deposition, nonuniform Zn morphology with some protuberances appears on the bare Zn surfaces. These protuberances remained and grew into needle-like dendrites in the following deposition process. In contrast, the deposition on FCOF@Zn is smooth as evidenced in Fig. **4**l. No obvious Zn dendrites were observed, even after 35 mins deposition. The microscopic morphologies of the Zn anodes after cycling at 1 and 5 $mAhcm^{-2}$, for 500h were also investigated. As shown in Supplementary Fig. 18, the FCOF@Zn anodes show that dendrite-free morphology and parallel platelet-morphology is consistently maintained. In contrast, protuberant Zn dendrites are found randomly distributed on bare Zn surfaces. Moreover, the HRTEM and FTIR results (Supplementary Fig. 19) show the FCOF films maintain good crystallinity and chemical structure stability after cycling. Consequently, it can be concluded that the multifunctional F nanochannels greatly improve the Zn^{2+} kinetics and deposition morphology, which results in high-rate and long life FCOF@Zn anodes.

Full cell performance and flexible device demonstration.

We next evaluated the electrochemical performance of full cells in which FCOF@Zn or Zn anodes were paired with high mass-loading (~8$mgcm^{-2}$) manganese dioxide (MnO_2) cathodes. For the FCOF@Zn/MnO_2cells, cyclic voltammetry curve (CV) curves demonstrated a larger current density at 0.1mVs^{-1} and a smaller voltage gap between typical redox peaks than in Zn/MnO_2 cells (Supplementary Fig. 20a). This implies that the FCOF@Zn/MnO_2 cells possessed higher specific capacity and better charge transfer capability[6]. EIS results further confirmed that, the impedance of the FCOF@Zn/MnO_2 cells (~100 Ω) is lower than that of Zn/MnO_2cells (Supplementary Fig. 20b). Therefore, at a current density of 3C, the FCOF@Zn/MnO_2 cells revealed a high initial reversible specific capacity of 130 $mAhg^{-1}$, while the

Zn/MnO_2 cells attained only 120 $mAhg^{-1}$ (Supplementary Fig. 20c). The FCOF films clearly endowed stable cycling of the Zn anodes, and retained a capacity of ~92 % and stable charge/discharge curves after 1000 cycles (Fig. **5**a and Supplementary Fig. 20d, e). This is nearly four times higher than the Zn/MnO_2 cells (capacity retention: 20%). Reducing the capacity ratio of the negative electrode to the positive electrode (N/P) during full cell operation is a key parameter to achieve high energy density[14,30,45]. In previous studies, many systems chose to use thick zinc foil (≥100um) paired with low mass loading cathodes to assemble full cells, the N/P reported in these studies is typically higher than 50, which is not beneficial for achieving high energy density. In our case, the excellent performance of the FCOF@Zn anodes allowed us to further evaluate the cycle performance of full cells under harsh conditions. Using thin FCOF film-protected Zn plates as anodes (the thin Zn plates is rolled to desired thickness to satisfy the required N/P condition), $FCOF@Zn/MnO_2$ cells with N/P=10:1 and N/P=5:1 showed stable specific capacity at current density of 4 $mAcm^{-2}$ for over 300 and 200 cycles, respectively (Fig. **5**b). The Zn platelet morphology after cycling and stable charge-discharge curves indicate the FCOF films enabled great performance improvements in Zn anodes (Supplementary Fig. 21). To evaluate the electrochemical performance of the aqueous Zn batteries for commercial applications under practical conditions, lean electrolyte addition and high areal capacity cathode is needed (inset of Fig. **5**c). Here, the electrolyte-to-capacity ratio (E/C) used was controlled at 12 μL mA h^{-1} and the MnO_2 mass loading was increased to 16 $mgcm^{-2}$. The assembled full cell still showed considerable capacity of 0.5 $mAhcm^{-2}$ after 250 cycles at a current density of 3$mAcm^{-2}$. The gravimetric energy density of the cell is 130Wh/kg (based on the total mass of the Zn anode and the MnO_2 cathode), which is significantly increased (by approx. 6.5 times) compared with many reported Zn/MnO_2 cells using low mass loading cathodes and thick Zn foils[30,39] (Fig. **5**d). It should be noted that the cell still delivered an energy density of 55Wh kg^{-1} when including the electrolyte weight. Further optimization of other key components such as separator membrane and electrolyte may improve the energy density of the cell.

To further demonstrate the application prospects of the FCOF@Zn anodes for constructing realistic, smart, high-performance aqueous Zn batteries, we assembled a flexible transparent battery for device demonstration. Fig. **5**e and Supplementary Fig. 22 shows the structural schematic diagram of the transparent battery. The MnO_2 cathode and FCOF@Zn anode are fixed to the flexible PVC substrate, and glass fiber is used as the separator. All layers are sandwiched and the battery is then assembled by thermal sealing. The cycling performance of the flexible battery under different bending conditions is shown in Fig. 5h-j. The EIS results (Supplementary Fig. 23) and the charge and discharge curves (insets of Fig. 5i, j) remain nearly unchanged at bending angles of 0°, 45° and 60°, respectively, indicating its good mechanical stability and flexibility. To create a more realistic scenario, a flexible $FCOF@ Zn/MnO_2$ battery was used to power a wearable bracelet for lighting a light emitting diode (LED) indicator (Fig. 5f, g), showing its promising application in portable wearable electronic devices.

Discussion

The excellent electrochemical performance of the FCOF@Zn anodes can be mainly attributed to the planar deposition morphology, *i.e.* the predominantly parallel tessellated Zn platelets. This specific morphology seems to result from the tailored strongly-electronegative F atoms within the FCOF films, since the surface stability of inorganic crystals is largely governed by their surface chemistry. The preference of the exposed the crystal plane is closely related to the surface energy changes[31-33]. Previous studies[31,46] indicated that the specific surface crystal planes in anatase surfaces are preferentially terminated by F atoms, inducing the anatase to expose specific crystal planes. Such a result is attributed to the surface energy decreases after the interaction between F and these crystal planes. The F terminated (FT) plane with lowest the surface energy tends to stay exposed instead of its intrinsic thermodynamically stable plane. In our case, the uniformly distributed F atoms within FCOF film have a strong binding interaction with the Zn atoms, thereby regulating the relative surface energy value of the (101) and (002) planes and influencing the deposited morphology. To verify this, the surface energy and adsorption energy of the two crystal planes terminated by F atoms are studied by first-principles calculations (Fig. **6**a). The calculated energy values clearly show that F atoms result in bonding to (002) planes that are more stable than (101) planes (Fig. **6**b), and F atoms interact more strongly with the (002) planes (Fig. **6**c), in accordance with the above XRD results. Moreover, with the formation of Zn-F interactions, the equilibrium positions of the Zn atoms on the surface of the crystal surface are clearly and obviously moved outward from where they would be without the presence of F atoms (insets of Fig. **6**b). To further elucidate the stability mechanisms associated with F atoms, the electronic structures of clean surfaces and FT surfaces are investigated. The PDOS of clean and fluorinated surfaces are shown in Fig. **6**d, e. For the clean surfaces, electrons contributed by Zn_{4s} delocalize in the range of the higher valence band (VB) and lower conduction band (CB). With the formation of Zn-F interaction, however, localized states of Zn_{4s} are observed, indicating that F atoms are prone to stabilize Zn atoms. To qualitatively determine the strength of the interaction between F atoms and Zn atoms and its impact on different crystal planes, the electron states of the Zn_{3d} and F_{2p} are analyzed. Due to the strong electron-withdrawing property of F atoms, the F_{2p} could accept electrons from the Zn_{4s}. As a result, the Zn_{4s} planes would partially lose electrons, forming quasi-stable bonds with the F species. Thereafter, the electrons from the Zn_{3d} may be excited toward the Fermi level. The displacement of Zn_{3d} electrons from the FT-(002) planes is more energetically-favourable than from FT-(101) planes. On the other hand, compared with the F_{2p} electron states of the in FT-(101) planes, the F_{2p} electron distribution in a FT-(002) plane is more localized. These results clearly suggest that F atoms interact more strongly with the (002) planes than with the (101) plane. The XPS data for the F_{1s} and Zn_{2p} at the FCOF-Zn interface also indicate the existence of strong F-Zn interaction[47-50] (Supplementary Fig. 24). Therefore, the FT-(002) planes are more stable and thus preferentially form the outer surfaces. It seems the (101) surfaces are preferentially eroded in a stepped fashion during electro-stripping so that the exposed surface which remains and subsequently builds up Zn deposits is a (002) surface.

Through experimental and first-principles calculations, we have determined that the F atoms in the FCOF film demonstrate the strongest interaction with the (002) crystal planes of Zn. The growth of (002) planes

is most stable during the deposition process, and anisotropic growth of Zn along other planes is done in such a way that a (002) plane is formed, resulting in platelet-like Zn deposits. Given that the F atoms bonded within the FCOF film are arranged in parallel along the surfaces of the current collectors, which induces each Zn platelet to also be arranged in parallel. Furthermore, the F-containing porous nano channels endow good hydrophobic effects on the film, which is beneficial for de-solvation and facilitates fast transport of hydrated Zn^{2+}, as well as reducing the corrosion of Zn by the aqueous electrolyte. The presence of F atoms and the “built-in nanochannels” in FCOF films seems to endow multiple advantages: the FCOF@Zn anodes exhibit excellent fast charging properties and cycle stability. The FCOF@Zn anodes can sustain over 320 cycles with excellent reversibility of ~97.2 % and the symmetric cells exhibit long cycle life up to 800h at an ultrahigh current density of 40mA cm^{-2}. This work provides novel design concepts for the realization of planar deposition and thus dendrite-free Zn anodes. Moreover, the 2D COFs films are versatile platforms that show distinct advantages for constructing high-performance batteries, owing to their adjustable pore sizes, tailored functional groups, light weight and structural stability through covalent bonding. The 2D COF rational design of the approach may also prove useful for other dendrite-free, long-life, and high-safety metal anode batteries, such as lithium, sodium, potassium and magnesium.

Methods

Preparation of FCOF films and MnO_2 cathodes. For the typical synthesis of FCOF film, a pyrex tube was charged with 3.75 mg (0.0182 mmol) 2, 3, 5, 6-tetrafluoroterephthalaldehyde (TFA), 4.40 mg (0.0125 mmol) 1,3,5-Tris(4-aminophenyl) benzene (TAPB), 1.8 mL dioxane (Dio) and 0.2 mL 1, 3, 5-trimethylbenzene (TMB). After sonication for 10 min, 0.1 mL HOAc (1.5 M) solution was added. After this, the tube was frozen at 77 K (liquid N_2 bath) and degassed by three freeze-pump-thaw cycles and finally sealed under vacuum conditions. The sealed tube was heated at 120^oC for 3 days. For the postprocessing, the tube was opened, washed with acetone several times and then the tube was charged with deionized water overnight. The free-standing FCOF films easily detach from the tube wall by gently shaking the tube. The obtained FCOF films were immersed in acetone for 2 days to wash out any impurities. Finally, the as-prepared FCOF films was transferred to various substrates via a pulling method in acetone solvent. The thickness of the membrane/film can be also easily tuned by controlling the concentration of monomers. The MnO_2 cathodes were synthesized using an aging method according to a previous report[51].

Structural and chemical characterizations. Wide-angle X-ray scattering (WAXS) measurement was conducted on a XenocsXeuss2.0 with 8KeV Cu Kα radiation. X-ray diffraction (XRD) data was measured by a Bruker D8 Advance with Cu-Kα X-ray radiation (λ = 0.154056 nm), using an operating voltage of 40 kV and a 40 mA current. Fourier transform infrared (FTIR) spectra were collected on a ThermoFisher Nicolet 6700 spectrometer. N_2 adsorption-desorption isotherms were measured at 77 K on a Micromeritics TriStar II 3020 volumetric adsorption analyzer after degassing in a vacuum at 120^oC was performed on a NT-MDT NTEGRA Spectra II microscope.

Field-emission scanning electron microscopy (FESEM) images were acquired from a Zeiss Gemini SEM500, equipped with an Aztec X-Max Extreme energy dispersive spectrometer (EDS). High-resolution Transmission Electron Microscope (HRTEM) images were collected from a JEM-2010F transmission electron microscope. XPS measurements were carried out with a Thermo Scientific K-Alpha + spectrometer under vacuum. Nano-indentation surface hardness measurements were conducted on a TI-950, NHT.

Electrochemical measurements. Cycling tests for symmetric cells and Zn/Ti half cells of bare Zn or FCOF@Zn were conducted with 2M $ZnSO_4$ aqueous electrolyte. For cathode fabrication, the high mass loading MnO_2 cathodes were prepared by mixing the active materials with carbon black and polytetrafluoroethylene (PTFE) in a mass ratio of 7:2:1. The mixture was compressed onto a Ti grid. The electrodes were dried at 80^oC under vacuum for 12h and then punched into disks. All the electrochemical properties were tested by assembling 2016-coin cells with glass fiber separators. All Galvanostatic charge-discharge measurements were carried out on a battery testing instrument (Land CT2001A, Wuhan China) at different current densities. Electrochemical impedance spectroscopy (EIS) and cyclic voltammetry (CV) were performed by a CHI 660E electrochemical workstation. CV curves of full cells were recorded over the voltage range of 1-1.85 V. EIS was measured in a frequency range of 100 kHz to 0.1 Hz at open circuit potential and an amplitude of 5 mV. The fitting parameters of the equivalent circuit were analyzed by ZSimpWin software.

Calculation method. The DFT calculations were carried out using the Vienna Ab-initio Simulation Package (VASP) with the frozen-core all-electron projector-augment-wave (PAW) method. The Perdew-Burke-Ernzerhof (PBE) form of the generalized gradient approximation (GGA) was adopted to describe the exchange and correlation potential. The cutoff energy for the plane-wave basis set was set to 500 eV. The Monkhorst-Pack k-point6 sampling was set to 3×3×1. The geometry optimizations were performed until the forces on each ion was reduced below 0.05 eV/Å. The vacuum slab models were used to calculate the adsorption of F atom on Zn(002) and (101) surfaces. These Zn surface slabs comprise 4 layers of Zn atoms, and a vacuum region of 20 Å above them was used to ensure the decoupling between neighboring systems. For the geometry optimization, the atoms in the 2-bottom layers of slab were fixed to their bulk positions.

The adsorption energy, E_{ads}, is calculated using the expression:

$$E_{ads} = E_{surface} + 16E_F - E_{F+surface}$$

where $E_{surface}$is the energy of the clean Zn surface, $E_F$represents the energy of the F atom, and $E_{F+surface}$represents the total energy of the adsorbed F/Zn system.

The surface free energy (γ), is calculated using the expression based on a previous study[31]:

$$\gamma = \frac{E^{slab} - NE_{Zn}^{bulk} - N_F E_F}{2A}$$

where,$E_{Zn}^{bulk}$is the energy per unit of Zn, $E^{slab}$is the total energy of the slab, $N$is the total number of unit Zn contained in the slab model, $N_X$is the number of adsorbed F atoms, $E_F = \frac{1}{2}E_{F-F}$–and E_{F-F} indicates the total energy of dimer F_2.

The adsorption energy, E_{ads}, is calculated using the expression:

$E_{ads} = E_{surface} + 16E_F - E_{F+surface}$

where $E_{surface}$is the energy of the clean Zn surface, E_F represents the energy of the F atom, and $E_{F+surface}$ represents the total energy of the adsorbed F/Zn system.

The surface free energy (γ), is calculated using the expression based on a previous study[31]:

$\gamma = \frac{E^{slab} - NE_{Zn}^{bulk} - N_F E_F}{2A}$

where, E_{Zn}^{bulk} is the energy per unit of Zn, E^{slab} is the total energy of the slab, $N$is the total number of unit Zn contained in the slab model, N_X is the number of adsorbed F atoms, $E_F = \frac{1}{2}E_{F-F}$–and E_{F-F} indicates the total energy of dimer F_2.

Declarations

Acknowledgements

The authors greatly appreciate the financial support from the 973 Project (2011CB605702), the National Science Foundation of China (51173027, 21875141), the Shanghai Key Basic Research Project (14JC1400600), Beijing National Laboratory for Condensed Matter Physics, Shanghai International Collaboration Research Project (19520713900).

Author contributions

H.L., J.G., C.P. and Z.G. conceived and designed the experiment and participated in writing and revising the paper. Z.Z. performed the electrochemical tests, analyzed the data, and wrote the manuscript. R.W. and Q.W. synthesized the samples and performed the characterizations of COF. T.W. performed the WAXS

measurements. B.H. performed the AFM measurements. J.Z. performed the Raman measurements. Y.L. and P.L. provided valuable advice on simulation results. All authors have read and approved the final paper.

Competing interests

The authors declare no competing interests.

References

1. Wang, F. et al. Highly reversible zinc metal anode for aqueous batteries. *Nat. Mater.* **17**, 543–549 (2018).
2. Yi, Z., Chen, G., Hou, F., Wang, L. & Liang, J. Strategies for the stabilization of Zn metal anodes for Zn-ion batteries. *Adv. Energy Mater.* **11**, 2003065 (2021).
3. Tang, B., Shan, L., Liang, S. & Zhou, J. Issues and opportunities facing aqueous zinc-ion batteries. *Energ. Environ. Sci.* **12**, 3288–3334 (2019).
4. Zhang, Q., Luan, J., Tang, Y., Ji, X. & Wang, H. Interfacial design of dendrite-free zinc anodes for aqueous zinc-ion batteries. *Angew. Chem. Int. Ed.* **59**, 13180–13191 (2020).
5. Zheng, J. et al. Reversible epitaxial electrodeposition of metals in battery anodes. *Science.* **366**, 645–648 (2019).
6. Xie, X. et al. Manipulating the ion-transfer kinetics and interface stability for high-performance zinc metal anodes. *Energ. Environ. Sci.* **13**, 503–510 (2020).
7. Hao, J. et al. An in-depth study of Zn metal surface chemistry for advanced aqueous Zn-ion batteries. *Adv. Mater.* **32**, 2003021 (2020).
8. Zhao, Z. et al. Long-life and deeply rechargeable aqueous Zn anodes enabled by a multifunctional brightener-inspired interphase. *Energ. Environ. Sci.* **12**, 1938–1949 (2019).
9. Yang, Q. et al. Hydrogen-substituted graphdiyne ion tunnels directing concentration redistribution for commercial-grade dendrite-free zinc anodes. *Adv. Mater.* **32**, 2001755 (2020).
10. Bayaguud, A., Luo, X., Fu, Y. & Zhu, C. Cationic surfactant-type electrolyte additive enables three-dimensional dendrite-free zinc anode for stable zinc-ion batteries. *ACS Energy Lett.* **5**, 3012–3020 (2020).
11. Cong, J. et al. Ultra-stable and highly reversible aqueous zinc metal anodes with high preferred orientation deposition achieved by a polyanionic hydrogel electrolyte. *Energy Stor. Mater.* **35**, 586–594 (2021).
12. Yang, H. et al. Constructing a super-saturated electrolyte front surface for stable rechargeable aqueous zinc batteries. *Angew. Chem. Int. Ed.* **59**, 9377–9381 (2020).
13. Zeng, Y. et al. Dendrite-free zinc deposition induced by multifunctional CNT frameworks for stable flexible Zn-ion batteries. *Adv. Mater.* **31**, 1903675 (2019).

14. Wang, S. et al. Lamella-nanostructured eutectic zinc-aluminum alloys as reversible and dendrite-free anodes for aqueous rechargeable batteries. *Nat. Commun.* **11**, (2020).
15. Zhang, H., Liu, X., Li, H., Hasa, I. & Passerini, S. Challenges and strategies for high-energy aqueous electrolyte rechargeable batteries. *Angew. Chem. Int. Ed.* **60**, 598–616 (2021).
16. Zhou, M. et al. Suppressing by-product via stratified adsorption effect to assist highly reversible zinc anode in aqueous electrolyte. *J. Energy Chem.* **55**, 549–556 (2021).
17. Du, W. et al. Challenges in the material and structural design of zinc anode towards high-performance aqueous zinc-ion batteries. *Energ. Environ. Sci.* **13**, 3330–3360 (2020).
18. Wang, Z. et al. A metal-organic framework host for highly reversible dendrite-free zinc metal anodes. *Joule.* **3**, 1289–1300 (2019).
19. Zheng, J. et al. Spontaneous and field-induced crystallographic reorientation of metal electrodeposits at battery anodes. *Sci. Adv.* **6**, b1122 (2020).
20. Zheng, J. & Archer, L. A. Controlling electrochemical growth of metallic zinc electrodes: toward affordable rechargeable energy storage systems. *Sci. Adv.* **7**, (2021).
21. Majuste, D. et al. Effect of organic impurities on the morphology and crystallographic texture of zinc electrodeposits. *Hydrometallurgy.* **169**, 330–338 (2017).
22. Nayana, K. O. & Venkatesha, T. V. Synergistic effects of additives on morphology, texture and discharge mechanism of zinc during electrodeposition. *J. Electroanal. Chem.* **663**, 98–107 (2011).
23. Raeissi, K., Saatchi, A., Golozar, M. A. & Szpunar, J. A. Texture and surface morphology in zinc electrodeposits. *J. Appl. Electrochem.* **34**, 1249–1258 (2004).
24. Yuan, D. et al. Anion texturing towards dendrite-free Zn anode for aqueous rechargeable batteries. *Angew. Chem. Int. Ed.* **133**, 7289–7295 (2021).
25. Sun, K. E. K. et al. Suppression of dendrite formation and corrosion on zinc anode of secondary aqueous batteries. *ACS Appl. Mater. Inter.* **9**, 9681–9687 (2017).
26. Hao, J. et al. Boosting zinc electrode reversibility in aqueous electrolytes by using low-cost antisolvents. *Angew. Chem. Int. Ed.* **60**, 7366–7375 (2021).
27. Kubo, B. et al. Effect of surface textures of iron substrate on the crystal orientation relationship between electrodeposited zinc and iron. *ISIJ Int.* **59**, 144–151 (2019).
28. KAMEI, K. & OHMORI, Y. Hetero-epitaxial growth of zinc electrodeposits on low-carbon steel sheets. *J. Appl. Electrochem.* **17**, 821–827 (1987).
29. Monzon, L. M. A., Klodt, L. & Coey, J. M. D. Nucleation and electrochemical growth of zinc crystals on polyaniline films. *J. Phys. Chem. C.* **116**, 18308–18317 (2012).
30. Hao, J. et al. Deeply understanding the Zn anode behaviour and corresponding improvement strategies in different aqueous Zn-based batteries. *Energ. Environ. Sci.*, (2020).
31. Yang, H. G. et al. Anatase TiO_2 single crystals with a large percentage of reactive facets. *Nature.* **453**, 638–641 (2008).

32. Maurer, F. et al. Preferred growth orientation of metallic fcc nanowires under direct and alternating electrodeposition conditions. *Nanotechnology.* **18**, 135709 (2007).
33. Pan, H., Sun, H., Poh, C., Feng, Y. & Lin, J. Single-crystal growth of metallic nanowires with preferred orientation. *Nanotechnology.* **16**, 1559–1564 (2005).
34. Liao, Q. et al. Catalyst-free and efficient fabrication of highly crystalline fluorinated covalent organic frameworks for selective guest adsorption. *J. Mater. Chem. A.* **7**, 18959–18970 (2019).
35. Zhou, D., Tan, X., Wu, H., Tian, L. & Li, M. Synthesis of C – C bonded two-dimensional conjugated covalent organic framework films by Suzuki polymerization on a liquid-liquid interface. *Angew. Chem. Int. Ed.* **58**, 1376–1381 (2019).
36. Zhao, R. et al. Redirected Zn electrodeposition by an anti-corrosion elastic constraint for highly reversible Zn anodes. *Adv. Funct. Mater.* **31**, 2001867 (2021).
37. Deng, C. et al. A sieve-functional and uniform-porous kaolin layer toward stable zinc metal anode. *Adv. Funct. Mater.* **30**, 2000599 (2020).
38. Zhao, Z. et al. Covalent organic framework-based ultrathin crystalline porous film: Manipulating uniformity of fluoride distribution for stabilizing lithium metal anode. *J. Mater. Chem. A.* **8**, 3459–3467 (2020).
39. Zeng, X. et al. Electrolyte design for in situ construction of highly Zn^{2+}-conductive solid electrolyte interphase to enable high-performance aqueous Zn-ion batteries under practical conditions. *Adv. Mater.* **33**, 2007416 (2021).
40. Wang, Y., Tang, W. & Zhang, L. Crystalline size effects on texture coefficient, electrical and optical properties of sputter-deposited Ga-doped ZnO thin films. *J. Mater. Sci. Technol.* **31**, 175–181 (2015).
41. Li, N. et al. Reduced-graphene-oxide-guided directional growth of planar lithium layers. *Adv. Mater.* **32**, 1907079 (2019).
42. Shi, F. et al. Strong texturing of lithium metal in batteries. *PNAS.* **114**, 12138–12143 (2017).
43. Kasperek, J. & Lenglet, M. Identification of thin films on zinc substrates by FTIR and Raman spectroscopies. *Rev. Met. Paris.* **94**, 713–719 (1997).
44. Raeissi, K., Golozar, M. A., Saatchi, A. & Szpunar, J. A. The effect of texture on the corrosion resistance of zinc electrodeposits. *T. I. Met. Finish.* **83**, 99–103 (2005).
45. Liu, J. et al. Pathways for practical high-energy long-cycling lithium metal batteries. *Nature Energy*. **4**, 180–186 (2019).
46. Liu, S., Yu, J. & Jaroniec, M. Anatase TiO_2 with dominant High-Energy {001} facets: Synthesis, properties, and applications. *Chem. Mater.* **23**, 4085–4093 (2011).
47. Waware, U. S., Hamouda, A. M. S., Rashid, M. & Kasak, P. Binding energy, structural, and dielectric properties of thin film of poly(aniline-co-m-fluoroaniline). *Ionics.* **24**, 3249–3257 (2018).
48. Xu, H. Y. et al. Photoluminescence of F-passivated ZnO nanocrystalline films made from thermally oxidized ZnF_2 films. *J. Phys. Condens. Matter.* **16**, 5143–5150 (2004).

49. Wang, H. et al. Synthesis and characterization of F-doped MgZnO films prepared by RF magnetron co-sputtering. *Appl. Surf. Sci.* **503**, 144273 (2020).
50. Ilican, S., Caglar, M., Aksoy, S. & Caglar, Y. XPS studies of electrodeposited grown F-Doped ZnO rods and electrical properties of p-Si/n-FZN heterojunctions. *J. Nanomater.* 2016, 1–9 (2016).
51. Qiu, N., Chen, H., Yang, Z., Sun, S. & Wang, Y. Low-cost birnessite as a promising cathode for high-performance aqueous rechargeable batteries. *Electrochim. Acta.* **272**, 154–160 (2018).

Figures

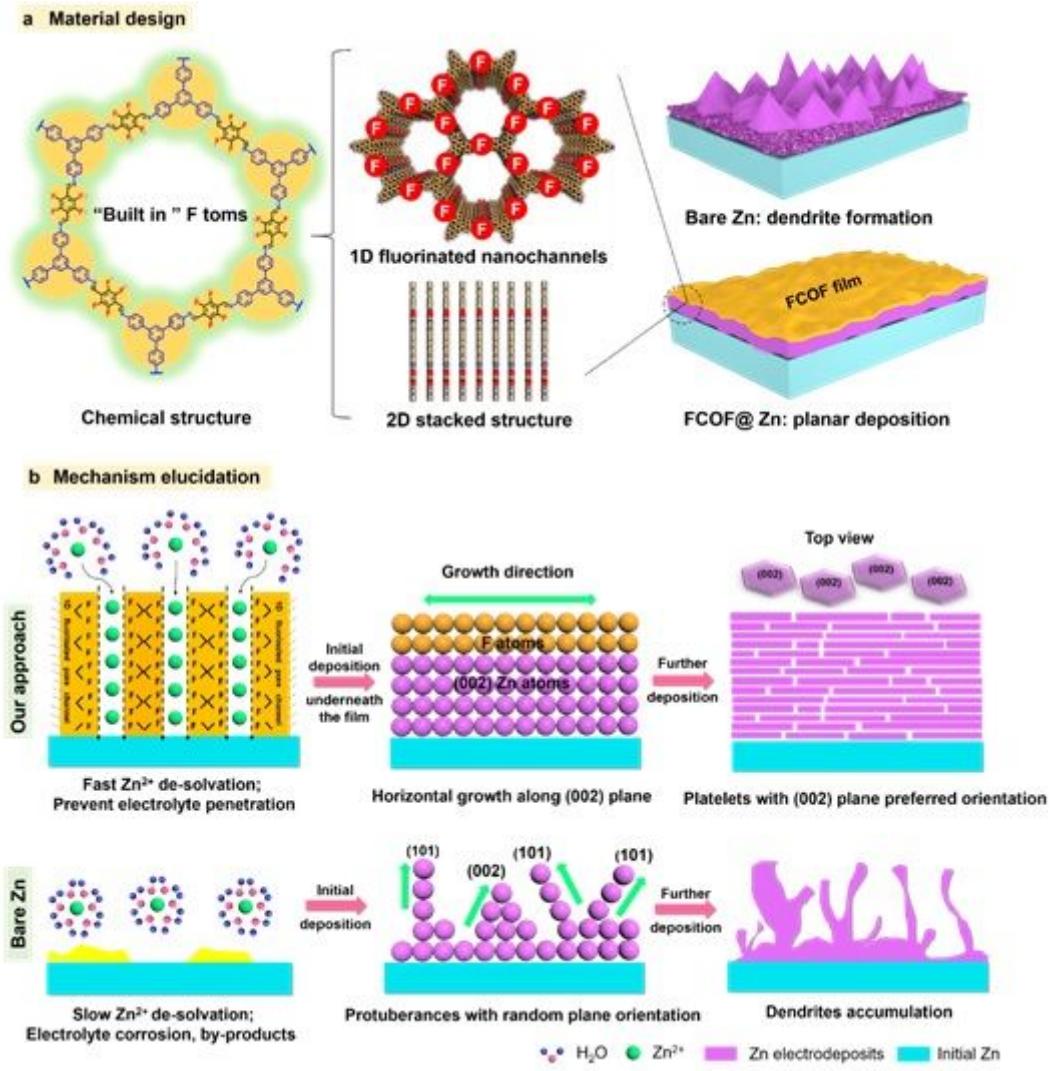

Figure 1

The schematic illustration of the planar Zn deposition morphology and the corresponding horizontal deposition mechanism elucidation enabled the FCOF film. a: The physicochemical structure of the FCOF film, showing suppression of dendrites. b: Mechanism comparison of the deposition processes for FCOF@Zn and bare Zn surfaces.

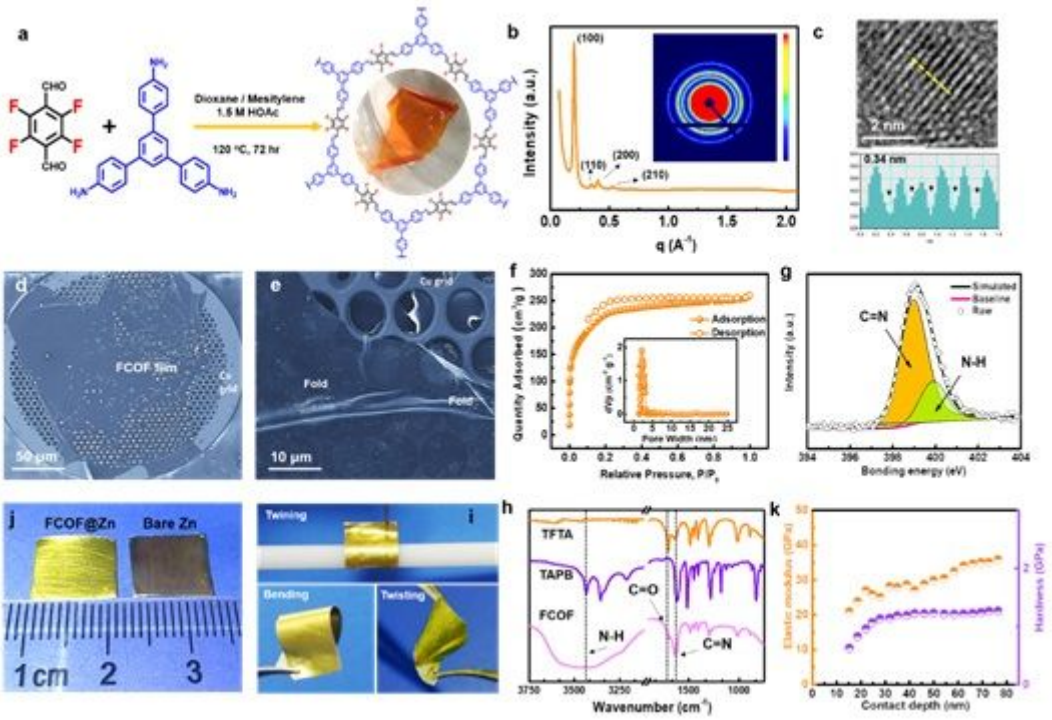

Figure 2

The morphology and structure characterization of the FCOF film. a: Synthesis procedure of the FCOF film. b: WAXS result and its integrated curve. c: HRTEM image and measurement of d-spacing. d-e: FESEM images of the FCOF film. f: BET measurement and pore size distribution. G: XPS result for N1s in the FCOF film. j-i: Pictures of typical FCOF@Zn and typical bare Zn. H: FTIR result for the monomers and the FCOF film. k: Nano-indentation measurement result for FCOF film.

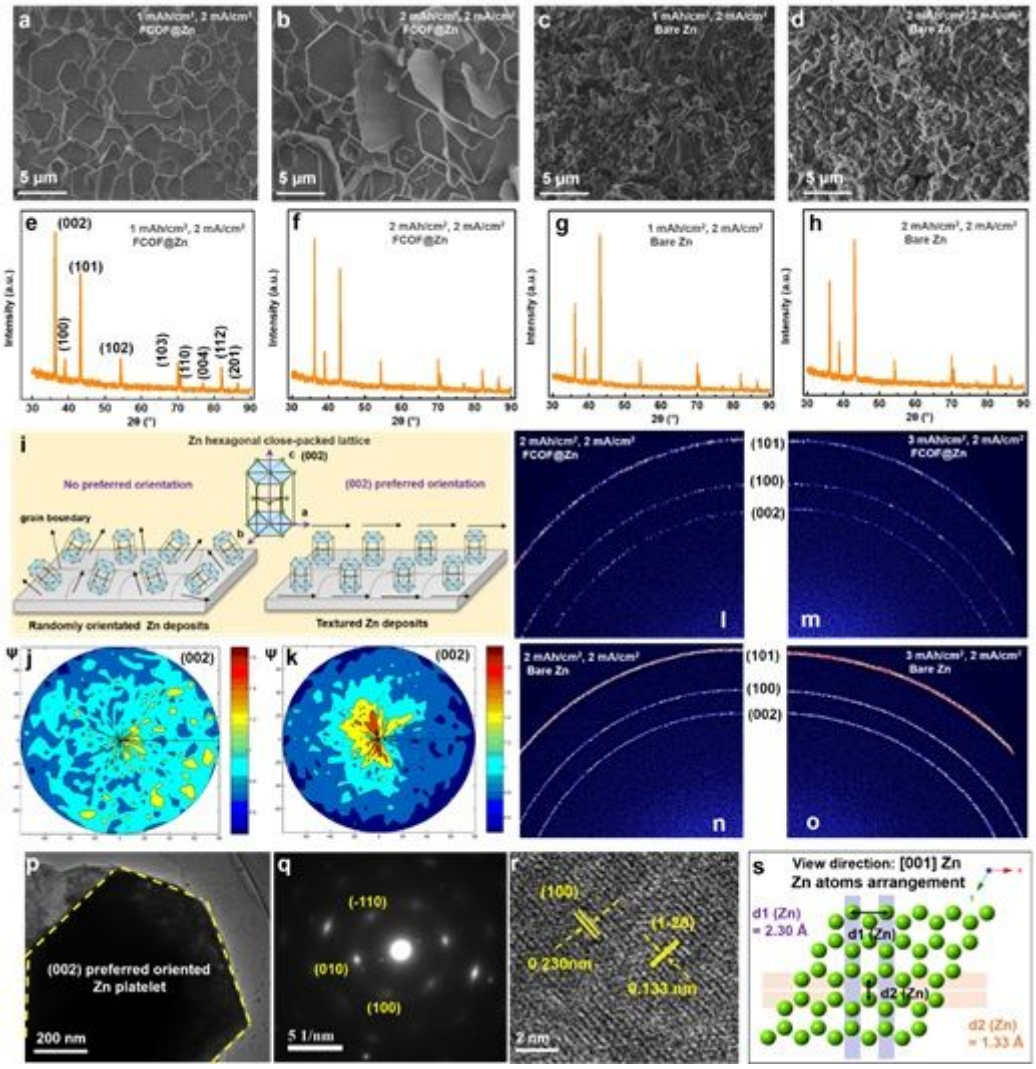

Figure 3

Morphology, crystallography and microstructure characterization of Zn electrodeposits. FESEM images of Zn deposits a-b: underneath a FCOF film and c-d: on bare Ti. XRD results for the Zn deposits e-f: underneath the FCOF film and g-h: on bare Ti. i: Schematic illustration of preferred orientations of Zn crystal plane. (002) plane pole figures of the Zn deposits j: on bare Ti and k: underneath FCOF film. The WAXS results of Zn deposits l-m: underneath FCOF film and n-o: on bare Ti. p-r: HRTEM images and SAED patterns of the Zn platelet. S: Theoretical atomic model of Zn along the [001] direction.

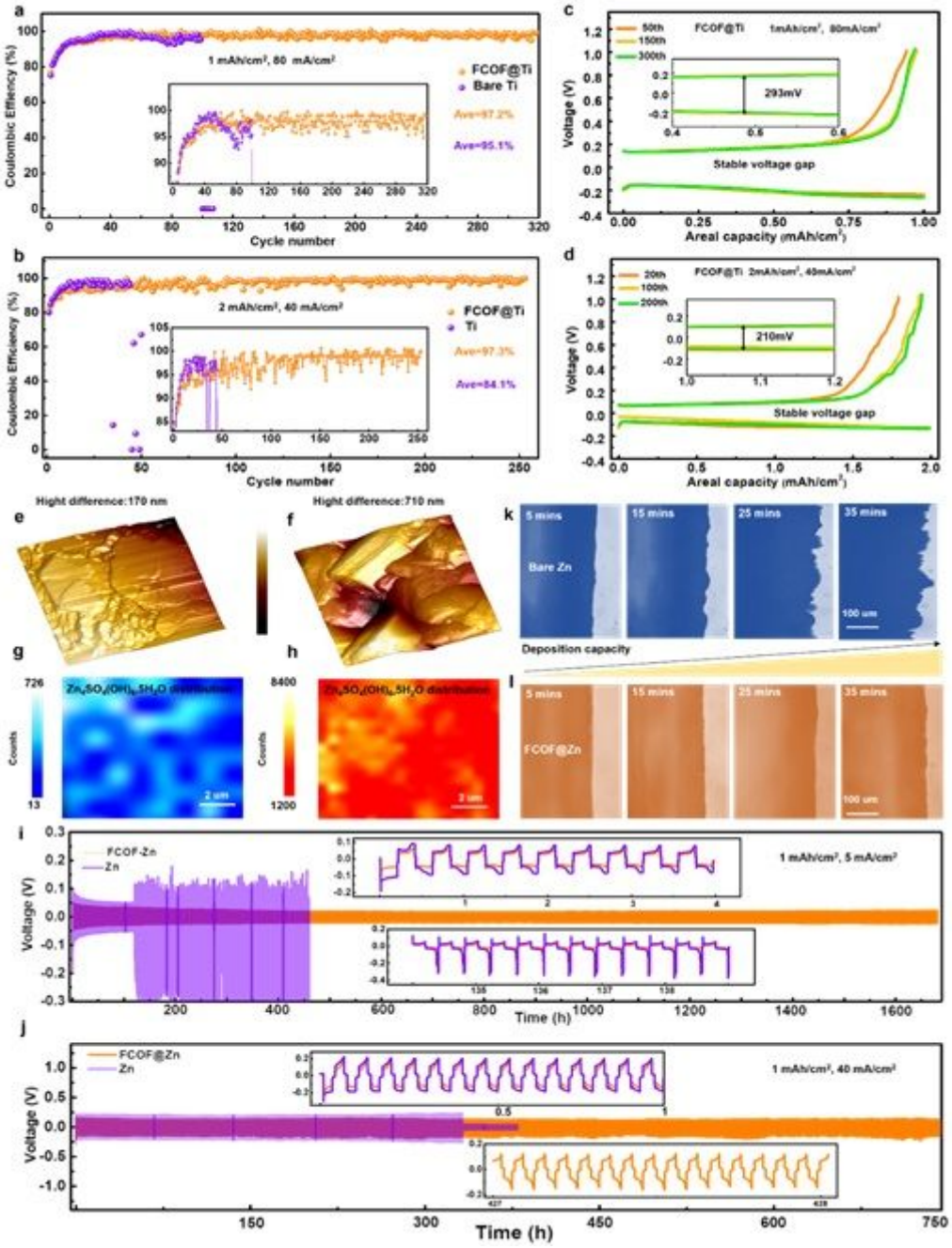

Figure 4

The electrochemical performance of Zn anodes. CE of Zn plating/stripping on FCOF film- coated Ti and bare Ti at a:1 mAh/cm2, 80 mA/cm2 and b: 2 mAh/cm2,40 mA/cm2. c-d: The corresponding voltage profiles at various cycles on FCOF film-coated Ti. The insets are enlarged voltage profiles. AFM 3D height imaging and 2D Raman mapping on the surfaces of Zn deposits after 200 cycles plating/stripping (1 mAh/cm2, 5 mA/cm2), e and g: on FCOF film- coated Ti and f and h: bare Ti. Cycling performance of Zn symmetric cells with or without FCOF film protection at i: 1 mAh/cm2, 5 mA/cm2, and j: 1 mAh/cm2, 40 mA/cm2. The insets are initial and selected voltage-time profiles. In situ optical microscopy studies on Zn deposition behaviors. k: Bare Zn, l: FCOF@Zn.

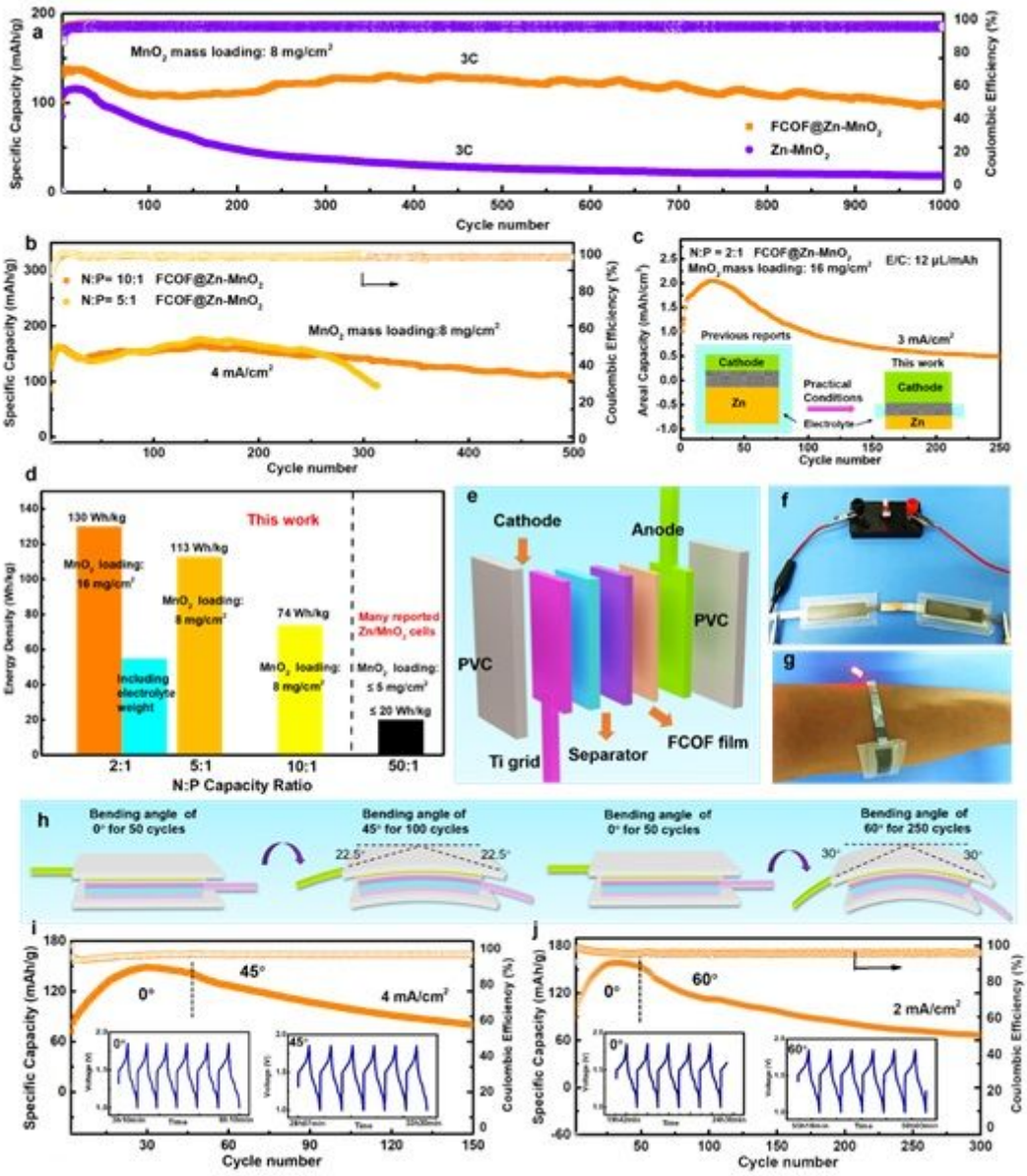

Figure 5

The full cell performance and flexible device demonstration. a: Cycling performance at current density of 3C. b: Cycling performance at N:P capacity ratio conditions of 10:1 and 5:1. c: Cycling performance at low N:P capacity ratio of 2:1 with controlled electrolyte addition of 12 μL/mA h-1 d: Dependence of cell-level energy density on N/P ratio in Zn/MnO2 full cell. The gravimetrical energy density is calculated based on the total mass of the Zn anode and the MnO2 cathode. e: Assembly schematic illustration of the flexible transparent battery. f-g: Pictures of the battery acting as a source of energy to power a LED. h-i: Cycling performance of the flexible transparent battery under different bending angles. The insets are selected voltage-time profiles.

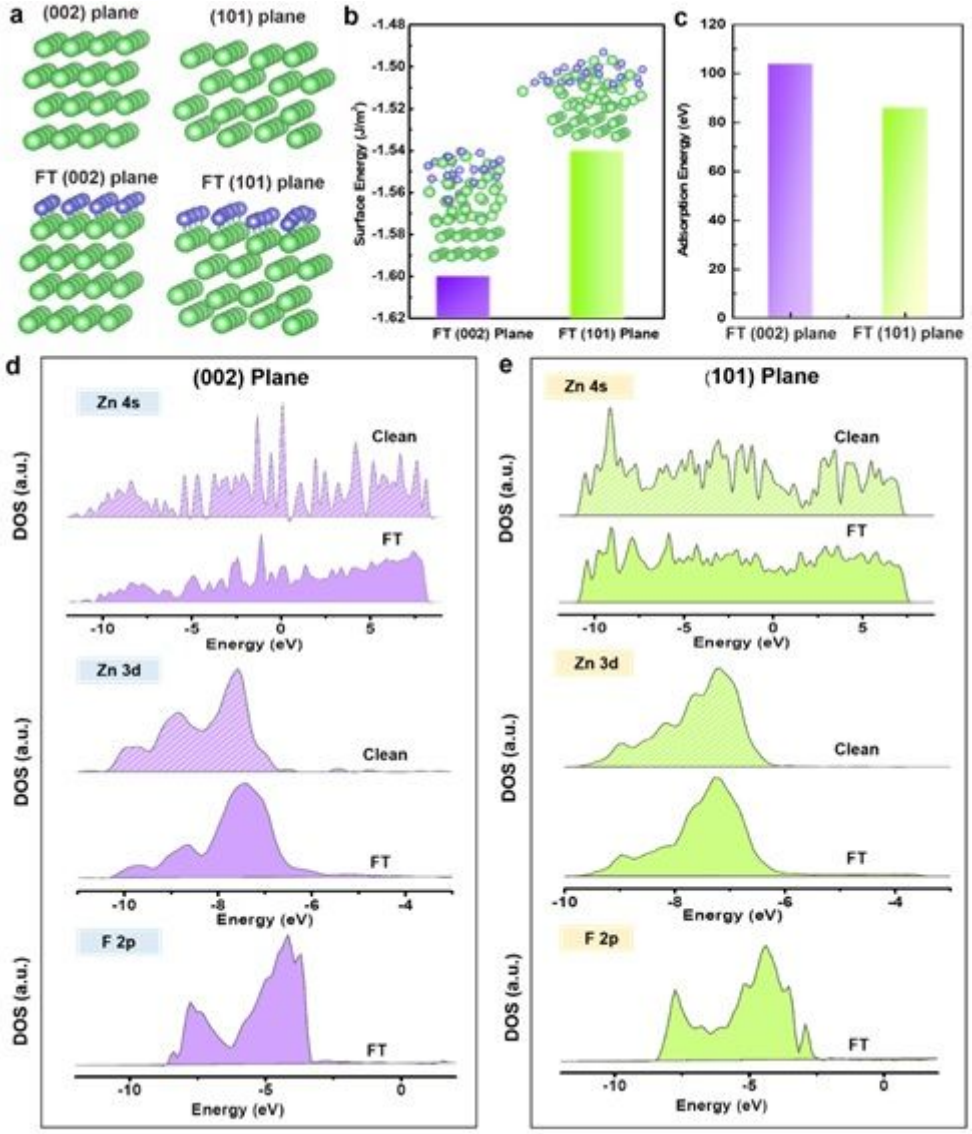

Figure 6

Theoretical simulation of FT-Zn (002) and FT-Zn (101). a: Calculations models of F atom adsorbed on Zn (002) and Zn (101). Calculated b: free energies and c: adsorption energies of F atom on Zn (002) plane and Zn (101) plane. d-e: Calculated projected density of states (PDOS) for clean Zn and FT-Zn systems.

Supplementary Files

This is a list of supplementary files associated with this preprint. Click to download.

- SupplementaryMaterials.docx
- SupplementaryMaterials.docx